Enhanced microscopic dynamics in mucus gels under a mechanical load in the linear viscoelastic regime

Domenico Larobina[a,1,2], Angelo Pommella[b,3], Adrian-Marie Philippe[b,4], Med Yassine Nagazi[b,5], and Luca Cipelletti[b,c,1,2]

[a]Institute of Polymers, Composites, and Biomaterials, National Research Council of Italy, Naples, 80055 Portici, Italy; [b]Laboratoire Charles Coulomb, Université Montpellier, CNRS, 34095 Montpellier, France; and [c]Institut Universitaire de France, 75231 Paris, France

Edited by David A. Weitz, Harvard University, Cambridge, MA, and approved September 19, 2021 (received for review February 28, 2021)

Mucus is a biological gel covering the surface of several tissues and ensuring key biological functions, including as a protective barrier against dehydration, pathogen penetration, or gastric acids. Mucus biological functioning requires a finely tuned balance between solid-like and fluid-like mechanical response, ensured by reversible bonds between mucins, the glycoproteins that form the gel. In living organisms, mucus is subject to various kinds of mechanical stresses, e.g., due to osmosis, bacterial penetration, coughing, and gastric peristalsis. However, our knowledge of the effects of stress on mucus is still rudimentary and mostly limited to macroscopic rheological measurements, with no insight into the relevant microscopic mechanisms. Here, we run mechanical tests simultaneously to measurements of the microscopic dynamics of pig gastric mucus. Strikingly, we find that a modest shear stress, within the macroscopic rheological linear regime, dramatically enhances mucus reorganization at the microscopic level, as signaled by a transient acceleration of the microscopic dynamics, by up to 2 orders of magnitude. We rationalize these findings by proposing a simple, yet general, model for the dynamics of physical gels under strain and validate its assumptions through numerical simulations of spring networks. These results shed light on the rearrangement dynamics of mucus at the microscopic scale, with potential implications in phenomena ranging from mucus clearance to bacterial and drug penetration.

mucus | rheology | dynamic light scattering | stress relaxation | microscopic dynamics

Mucus is a biogel ubiquitous across both vertebrates and invertebrates (1–3). The main mucus macromolecular components are a family of glycosylated proteins called mucins (4–6). Hydrophobic, hydrogen-bonding, and Ca^{2+}-mediated (7) interactions between mucins are responsible for macromolecular associations determining the viscoelastic properties of mucus, which, in turn, control its biological functions (2, 5). Alteration of the viscoelastic properties compromises mucus functionality, resulting in severe diseases (8, 9).

Mucus viscoelasticity stems from the reversible nature of the bonds between its constituents, which ensure solid-like behavior on short time scales while allowing flow on longer time scales. Rheological studies on mucus reporting the frequency dependence of the storage, G', and loss, G'', components of the dynamic modulus reveal $G' > G''$, with G' only weakly dependent on angular frequency ω on time scales of 0.1 to 100 s (8–10), a behavior typical of soft solids (11). Stress-relaxation tests probe viscoelasticity on longer time scales, up to thousands of seconds. They reveal a power law or logarithmic decay of the shear stress with time (12–14), indicative of a wide distribution of relaxation times, ascribed to the variety of macromolecular association mechanisms and the mucus complex, multiscale structure (7, 14, 15).

Alongside conventional rheology, microrheology has gained momentum since it investigates the mechanical response of mucus on the length scales relevant to its biological functions, from a fraction of a micrometer up to ~ 10 μm (7, 8, 16–19). Microrheology infers the viscoelastic moduli from the microscopic dynamics of tracer particles embedded in the sample (20), either due to spontaneous thermal fluctuations or externally driven, e.g., by a magnetic field. Mucus viscoelasticity as measured by microrheology is found to depend on the size of the tracer particles, the local environment they probe, and the length scale over which their motion is tracked (7, 8, 16, 17, 19, 21). Below ≈ 1 μm, microrheology data are dominated by the diffusion of the probe particles within the mucus pores, as inferred from the analysis of the localization of the tracers' trajectories (7, 17), their dependence on probe size (8, 16, 21), and on the amplitude of the external drive in active microrheology (16). On larger length scales, microrheology reports the local viscoelasticity, which converges toward the macroscopic one above ≈ 10 μm, as revealed by the probe-size and drive-amplitude dependence of active microrheology (16).

In vivo, mucus is submitted to stresses of various origin, involving strain on the microscopic scale, as in cilia beating in muco-ciliary clearance (22) and bacterial penetration (23, 24),

Significance

Mucus is a biological gel protecting several tissues. Its key properties result from a crucial balance between solid-like and fluid-like behavior, ensured by the nonpermanent nature of the bonds between its macromolecular constituents. Our understanding of the micrometer-scale response of mucus to an applied stress is still rudimentary, although in living organisms, stresses acting on mucus are ubiquitous, from bacterial penetration to coughing and peristalsis. We show that under a modest applied stress, in the mechanical linear regime, the microscopic dynamics of pig gastric mucus transiently accelerate by up to 2 orders of magnitude. A simple model rationalizes this previously unrecognized fluidization mechanism stemming from elastic recoil following bond breaking and generalizes our findings to networks with reversible bonds.

Author contributions: D.L. and L.C. designed research; D.L., A.P., A.-M.P., and L.C. performed research; M.Y.N. contributed to the model; D.L., A.P., M.Y.N., and L.C. analyzed data; and D.L. and L.C. wrote the paper.

The authors declare no competing interest.

This article is a PNAS Direct Submission.

[1]D.L. and L.C. contributed equally to this work.

[2]To whom correspondence may be addressed. Email: domenico.larobina@cnr.it or luca.cipelletti@umontpellier.fr.

[3]Present address: Université Lyon, Institut National des Sciences Appliqueés Lyon, CNRS, Matériaux: Ingénierie et Science, UMR5510, F-69621 Villeurbanne, France.

[4]Present address: Materials Research and Technology Department, Luxembourg Institute of Science and Technology, L-4422 Belvaux, Luxembourg.

[5]Present address: Formulaction, 31200 Toulouse, France.

This article contains supporting information online at https://www.pnas.org/lookup/suppl/doi:10.1073/pnas.2103995118/-/DCSupplemental.

Published November 2, 2021.

up to macroscopic scales, e.g., during coughing and peristalsis (3, 25). Stresses due to the osmotic pressure exerted by the environment (26) or resulting from changes in hydration (27, 28) can modify the structure of mucus and, e.g., impair mucus clearance. By contrast, little is known on the impact of stress on the dynamics of mucus, in particular, at the microscopic level. Conventional rheology indicates that mucus is fluidized upon applying a large stress (29, 30), beyond the linear regime. This behavior is typical of soft solids (31–33); in concentrated nanoemulsions and colloidal suspensions and in colloidal gels, fluidization in the nonlinear regime has been shown to stem from enhanced microscopic dynamics (34–40). However, for mucus, we still lack knowledge of the effect of an applied stress on the microscopic dynamics.

Here, we couple rheology and light and X-ray photon correlation methods to investigate the microscopic dynamics of pig gastric mucus under an applied shear stress. Surprisingly, we find that small stresses, well within the macroscopic linear viscoelastic regime, transiently enhance the mucus dynamics by up to 2 orders of magnitude. We propose a simple, yet general, model for the dynamics of physical gels under strain that rationalizes these findings.

Results

Range of Linear Viscoelasticity. We measure the viscoelastic properties of mucus gels under shear and use oscillatory rheometry and stress-relaxation tests to determine the range of the operational linear viscoelastic regime, where the viscoelastic moduli do not depend on the applied strain or stress. Fig. 1*A* shows the strain-amplitude dependence of the first harmonic of G' and G'' in oscillatory tests at a frequency of $\omega = 6.28\ \mathrm{rad}\cdot\mathrm{s}^{-1}$. Data have been normalized and averaged over several samples; typical values of the elastic modulus are in the range 20 to 200 Pa (*SI Appendix*). Both G' and G'' are independent of the strain amplitude up to $\gamma \approx 10\%$, beyond which the gel gradually deviates from linear response, with a global tendency toward fluidization. Up to $\gamma = 20\%$, deviations of the viscoelastic moduli with respect to their $\gamma \to 0$ value are smaller than 10%, as confirmed by measurements at various ω (*SI Appendix*). We probe the gel response on a wider range of time scales in stress-relaxation tests, where a step strain of amplitude γ_0 is applied at $t = 0$, and $\sigma(t)$, the time evolution of the stress needed to maintain such a deformation, is followed for up to 2,000 s. Fig. 1*B* shows the relaxation modulus $G(t) = \sigma(t)/\gamma_0$ for four strain amplitudes $\leq 20\%$. The decay of $G(t)$ is close to logarithmic, confirming a wide distribution of relaxation times, a behavior similar to that reported in other soft solids [alginate gels (41–43), granular media under compression (44, 45), and colloidal glasses in creep tests (46, 47)]. While the applied strain changes by a factor of 40, all $G(t)$ curves superimpose, indicating linear viscoelastic behavior up to $\gamma_0 = 20\%$. This is also confirmed by the amplitude of higher-order harmonics in oscillatory tests, a quantity widely used to characterize nonlinear behavior (30, 48), which shows no significant strain dependence up to $\gamma \gtrsim 30\%$ (*SI Appendix*). Thus, rheology data collectively indicate marginal, if any, deviations from linear viscoelastic behavior for $\gamma \leq 20\%$.

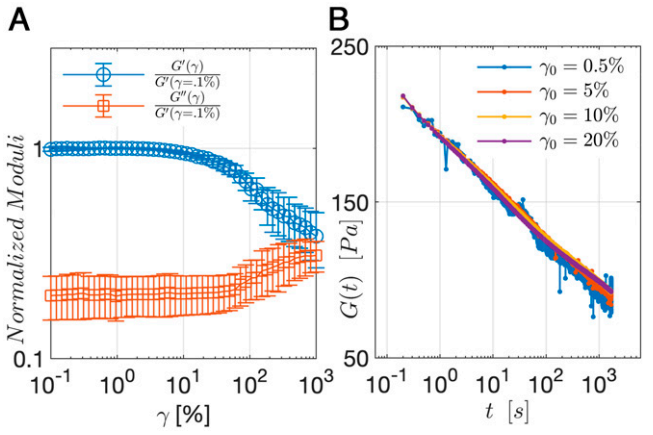

Fig. 1. Viscoelastic properties of pig gastric mucus gels. (*A*) Normalized storage (circles) and loss (squares) moduli vs. applied strain in oscillatory shear rheology tests at a frequency $\omega = 6.28$ rad · s^{-1}. Symbols: average over eight samples of the moduli normalized by G' at the smallest strain. Error bars: SD over the set of probed samples. (*B*) Relaxation modulus following a step-strain increment of amplitude γ_0, demonstrating linear behavior up to 20%.

Applying a Shear Strain Dramatically Accelerates the Microscopic Dynamics. Fig. 2*A* shows the microscopic dynamics of a mucus gel at rest (no applied strain), as probed by X-ray photon correlation spectroscopy (XPCS; *Materials and Methods*). Intensity correlation functions $g_2(\tau) - 1$ are measured at several scattering vectors q (49). This allows us to probe the relaxation time of the gel density fluctuations on length scales $\sim \pi/q$ spanning almost

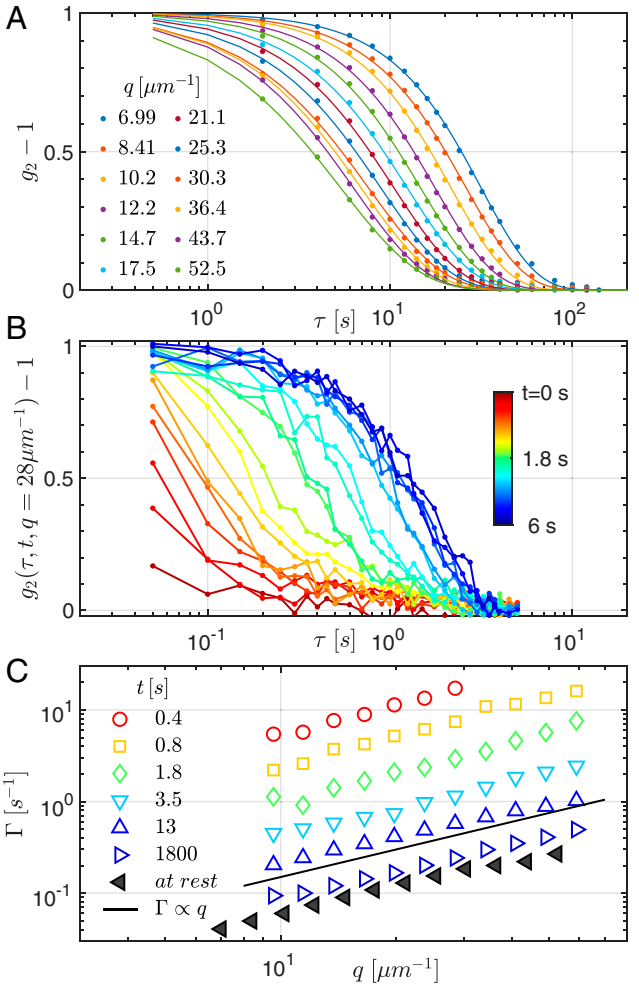

Fig. 2. Spontaneous and stress-induced dynamics probed by XPCS. (*A*) Intensity correlation functions for a mucus gel at rest, probed on length scales q^{-1} from 0.053 μm to 0.33 μm. (*B*) Two-times intensity correlation functions for $q = 28.5\ \mu\mathrm{m}^{-1}$ display a transient acceleration following a step strain with $\gamma_0 = 14.25\%$. Color code: time t after applying the step strain. (*C*) Open symbols: decay rate of $g_2 - 1$ vs. wave-vector q, for various t, as defined in *B*. Black filled triangles: relaxation rate for the sample at rest of *A*. The line shows the $\Gamma \propto q$ scaling expected for ballistic dynamics.

1 decade, from 0.053 μm to 0.33 μm, smaller than, but close to, ≈3 μm, the length scale beyond which the gel structure changes from fractal-like to rather uniform (14). The full decay of $g_2(\tau) - 1$ indicates that the network bonds are not permanent, consistent with the scenario based on previous measurements on mucus gels at lower q vectors (14). Data are well fitted by a generalized exponential decay, $g_2(\tau) - 1 = \exp[-(\Gamma\tau)^\beta \ln 2]$, where Γ is the half-decay rate defined by $g_2(1/\Gamma) - 1 = 0.5$ and β controls the shape of the decay. Over the probed q range, we find $\beta = 1.22 \pm 0.15$ and $\Gamma \propto q^a$, with $a = 0.94 \pm 0.06$ (filled triangles in Fig. 2*C*). Both the compressed exponential shape ($\beta > 1$) and the nearly linear dependence of the relaxation rate with q ($a \approx 1$) have been reported for a variety of soft solids, including biological gels (14, 41, 50–53). They are indicative of ballistic dynamics, as opposed to the diffusive motion usually observed in polymeric and colloidal systems at thermodynamic equilibrium (49, 54, 55), and have been attributed to the slow relaxation of internal stresses in amorphous, out-of-equilibrium soft solids (50, 56, 57). Consistent with this picture, we have shown in previous work that the spontaneous dynamics of mucus slow down over several hours (14), a behavior known as physical aging and typical of out-of-equilibrium amorphous materials. On time scales shorter than those accessible to XPCS, thermal fluctuations induce overdamped fluctuations of the gel at fixed network connectivity, in analogy to colloidal and polymeric gels (58–60). Dynamic light scattering (DLS) reveals that these fast relaxation modes have a characteristic time $\lesssim 1$ ms and that they account for less than 15% of the full relaxation of $g_2 - 1$ (*SI Appendix*).

Upon applying a step strain $\gamma_0 = 14.25\%$, within the linear viscoelastic regime, the mucus microscopic dynamics are dramatically enhanced. This is exemplified by Fig. 2*B*, which displays two-times intensity correlation functions (*Materials and Methods*) at a fixed q vector, for various times t after the step strain. We carefully checked that this acceleration does not stem from a spurious motion of the rheometer tool. Immediately after shearing the gel ($t = 0.05$ s; dark red curve in Fig. 2*B*), the dynamics are so fast that the decay of $g_2 - 1$ is barely measurable; subsequently, the decay rate progressively decreases, approaching that of a gel at rest. The dramatic impact of the applied strain on the microscopic dynamics has to be contrasted with the unchanged mechanical properties of the gel, since $\gamma_0 = 14.25\%$ falls within the linear viscoelastic regime (Fig. 1*B*). Fig. 2*C* shows that the applied strain transiently accelerates the dynamics by more than a factor of 50 at all q, i.e., at all probed length scales. Remarkably, the same dependence of the relaxation rate with q is seen during the dynamic acceleration as for the unperturbed gel, since we find $\Gamma \propto q^a$ with $a = 1.02 \pm 0.1$ averaged over the datasets with open symbols of Fig. 2*B*. This suggests that a similar mechanism may be responsible for the dynamics in both cases, i.e., the relaxation of stress acting on the gel, be it internal (as for the unperturbed samples) or externally applied.

Microscopic Dynamics Correlate with Stress Relaxation. To elucidate the relationship between microscopic dynamics and stress relaxation, we perform simultaneous rheology and DLS measurements on mucus gels using a custom setup (61) (*Materials and Methods*) that probes a scattering vector $q = 33\ \mu\text{m}^{-1}$, comparable to those in the XPCS experiments. Unlike in microrheology experiments, the DLS measurements probe the mucus gels with no added tracer particles. This avoids complications in the data analysis arising when the tracer particles are not fully slaved to the network dynamics, e.g., if they diffuse through the gel pores (7, 16, 17).

Strain ramps: Effect of strain rate. In a first series of experiments, we submit the mucus gels to strain ramps attaining the same final amplitude, $\gamma_0 = 20\%$, but at various strain rates $0.001\ \text{s}^{-1} \leq \dot{\gamma} \leq 0.04\ \text{s}^{-1}$. Fig. 3*A* shows the stress relaxation following the strain ramp, with $t = 0$ as the time at which the final strain is attained. At large t, all data follow the same trend, close to the logarithmic decay seen in Fig. 1*B* for a step strain. At earlier times, σ tends to a plateau, which becomes more pronounced as $\dot{\gamma}$ decreases. This behavior is rationalized by recalling that bonds within the mucus gel continuously break and reform and that stress relaxation occurs on a wide range of time scales. Accordingly, part of the stress generated during the ramp is actually relaxed before attaining the final deformation, through the fastest relaxation mechanisms. This scenario is supported by the fact that all the $\sigma(t)$ data collapse onto a master curve when plotting the stress as a function of an effective relaxation time $t + t_{shift}(\dot{\gamma})$, with t_{shift} proportional to the time $\gamma_0/\dot{\gamma}$ spent during the ramp (Fig. 3*A*, *Insets*).

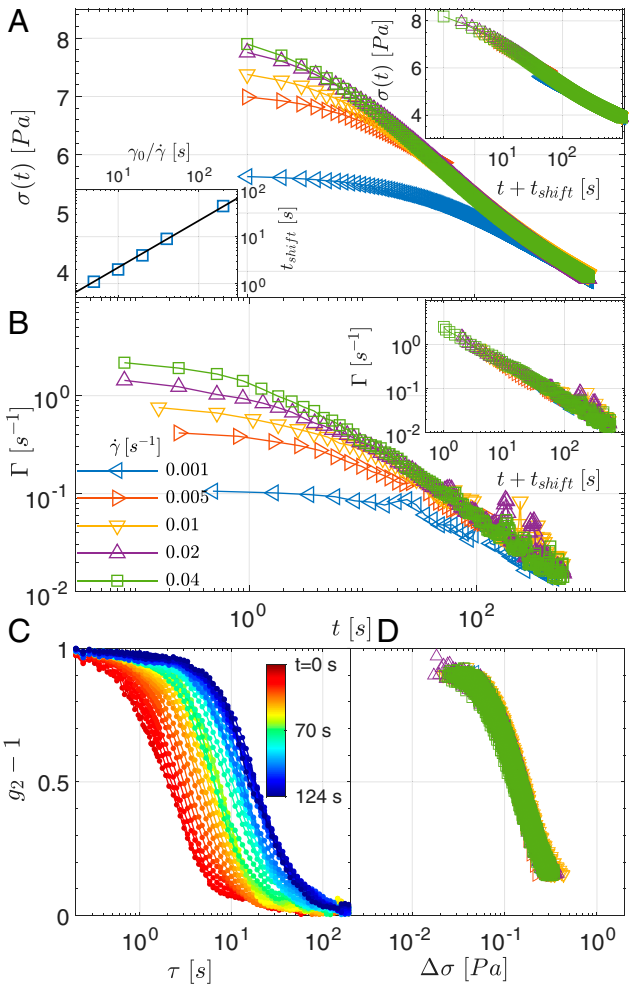

Fig. 3. Enhanced microscopic dynamics following a short strain ramp at a variable strain rate. Rheology and microscopic dynamics in stress-relaxation tests after reaching a fixed strain increment $\gamma_0 = 20\%$ through strain ramps at various rates $0.001 \leq \dot{\gamma} \leq 0.04\ \text{s}^{-1}$. In all panels, $t = 0$ at the end of the ramp. (*A*) Time-dependent stress relaxation. (*A*, *Upper Inset*) Collapse of the same data when plotted vs. the effective time $t + t_{shift}$. t_{shift} is proportional to the time $\gamma_0/\dot{\gamma}$ spent during the ramp, as shown by *A*, *Lower Inset*, where the line is a linear fit to the data, $t_{shift} = 0.22\gamma_0/\dot{\gamma}$. (*B*) Relaxation rate of the microscopic dynamics measured by DLS at $q = 33\ \mu\text{m}^{-1}$ after the strain increment; color code is as in *A*. (*B*, *Inset*) Same data plotted vs. shifted time, using the same t_{shift} as in *A*. (*C*) Representative correlation functions displaying faster decays after a strain ramp at $\dot{\gamma} = 0.005\ \text{s}^{-1}$. (*D*) In the accelerated regime ($\Gamma \geq 0.09\ \text{s}^{-1}$), the intensity correlation functions following ramps at all $\dot{\gamma}$ collapse onto a master curve when plotted vs. the stress drop $\Delta\sigma = \sigma(t) - \sigma(t + \tau)$.

We now turn to the microscopic dynamics. Fig. 3*C* shows an example of enhanced dynamics, representative of the general behavior. We find the relaxation rate to be markedly accelerated right after attaining the final strain amplitude, after which the microscopic dynamics slow down, in qualitative analogy to the XPCS measurements following a step strain (Fig. 2*B*). We plot in Fig. 3*B* the time-dependent relaxation rate of the microscopic dynamics for all ramps. Remarkably, $\Gamma(t)$ exhibits the same behavior as the stress relaxation: All data collapse at large t, while they tend to plateau at earlier times. As for $\sigma(t)$, the Γ plateau is more pronounced for the slower ramps. Finally, the inset of Fig. 3*B* shows that all the microscopic dynamics data collapse onto a master curve when plotting Γ vs. the effective relaxation time, using the same time shifts t_{shift} determined for the rheology data.

The strong analogies between the time evolution of the stress and that of the microscopic relaxation rate suggest that the macroscopic mechanical relaxation and the microscopic dynamics are intimately related. We make this observation quantitative by plotting in Fig. 3*D* the two-times correlation functions $g_2(t,\tau)-1$ in the accelerated regime, defined by $\Gamma \geq 0.09\ \mathrm{s}^{-1}$, as a function of the stress drop $\Delta\sigma = \sigma(t) - \sigma(t+\tau)$, rather than the time delay τ. Remarkably, data for all $\dot{\gamma}$ and all t during the acceleration phase collapse onto a master curve, demonstrating that the microscopic dynamics depend only on the stress drop, regardless of the strain history imposed to the sample. At longer times, when Γ drops below $0.09\ \mathrm{s}^{-1}$, the collapse of g_2-1 with $\Delta\sigma$ does not hold anymore, suggesting that the externally imposed stress has sufficiently relaxed for the microscopic dynamics to be dominated by the underlying spontaneous dynamics, which is ruled by the relaxation of internal stress, as in gels at rest.

Strain steps: Effect of strain amplitude. We establish the generality of the relationship between stress relaxation and microscopic dynamics in mucus gels by measuring the time evolution of both quantities after imposing a step strain of variable amplitude, $0.24\% \leq \gamma_0 \leq 9.84\%$, well within the linear viscoelastic regime. The experiments are performed simultaneously on the same sample, taking advantage of the plate–plate geometry of our setup, where the local strain varies linearly with distance from the rotation axis and where the local dynamics can be measured by space-resolved DLS (61, 62) (*Materials and Methods*).

Fig. 4 contrasts the dynamics for the smallest strain, $\gamma_0 = 0.24\%$ (Fig. 4*A*), with those for one of the largest strains, $\gamma_0 = 7.44\%$ (Fig. 4*B*). For the former, the applied step strain has no measurable effect on the decay of g_2-1, which occurs at the same rate as for the unperturbed sample and exhibits strong fluctuations, a distinctive feature of the spontaneous dynamics of mucus gels (14). At larger γ_0, by contrast, the dynamics are transiently enhanced, similarly to the XPCS and strain-ramp experiments (Figs. 2 and 3, respectively). The temporal evolution of the microscopic relaxation rate Γ is shown in Fig. 4*C* for all the tested γ_0. The transient acceleration lasts about 15 s; its magnitude grows with the amplitude of the applied strain, up to more than a 100-fold increase of the microscopic relaxation rate for $\gamma_0 = 9.84\%$ and $t = 0.1$ s. Fig. 4*D* shows that all correlation functions measured during the accelerated phase collapse onto a single master curve when plotting them vs. the stress decay $\Delta\sigma$, regardless of the applied strain. Thus, the scaling of g_2-1 with $\Delta\sigma$ is robust, not only with respect to a change of the strain-ramp rate, as demonstrated by Fig. 3, but also upon changes of the amplitude of the imposed strain.

Modeling the Relationship between Microscopic Dynamics and Stress Relaxation

We propose a simple model that rationalizes the relationship between the microscopic dynamics and the macroscopic stress relaxation. The main ingredients of the model are outlined here:

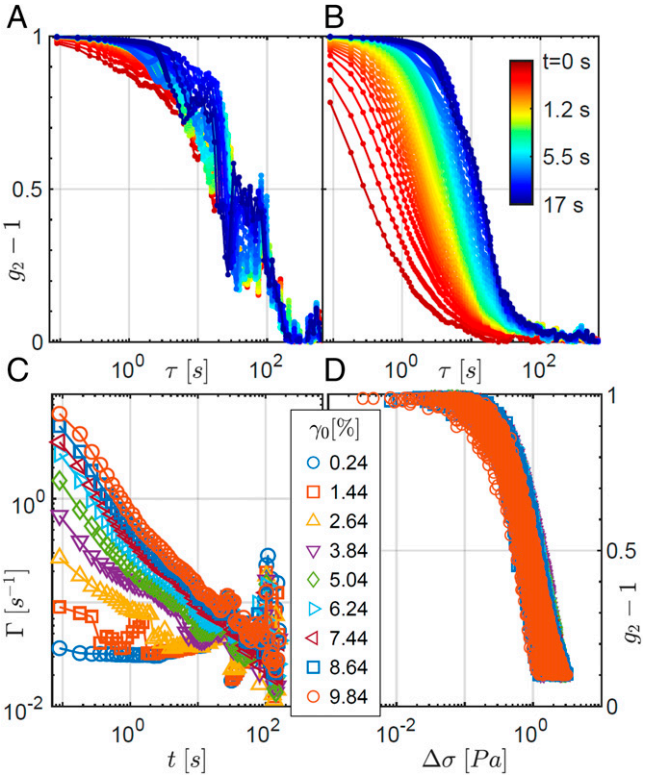

Fig. 4. Enhanced microscopic dynamics after strain steps of various amplitude. (*A* and *B*) Intensity correlation functions at $q = 33\ \mu\mathrm{m}^{-1}$ after strain steps with $\gamma_0 = 0.24\%$ (*A*) and $\gamma_0 = 7.44\%$ (*B*). The time t after the step is indicated in both panels by the color code of the bar in *B*. (*C*) Time dependence of the relaxation rate of the microscopic dynamics, after strain steps at various γ_0, shown in percent by the labels between *C* and *D*. (*D*) Master curve when plotting all correlation functions in the accelerated regime ($\Gamma \geq 0.09\ \mathrm{s}^{-1}$ and $\gamma_0 \geq 1.44\%$) vs. the stress drop $\Delta\sigma = \sigma(t) - \sigma(t+\tau)$. Symbols are the same as in *C*.

See *Materials and Methods* and *SI Appendix* for more details. The model focuses on the accelerated network dynamics upon applying a shear strain; it neglects the fast dynamics ($\Gamma \gtrsim 100\ \mathrm{s}^{-1}$) due to gel fluctuations at fixed network connectivity, as well as the spontaneous slow dynamics ($\Gamma \lesssim 0.09\ \mathrm{s}^{-1}$) that occur even in the absence of an applied strain. As indicated by the spontaneous dynamics and the rheology data, bonds within the gel network are continuously broken and reformed. In between a bond breaking and the following bond formation, the network relaxes its configuration so as to minimize the elastic energy. We shall term "rearrangement event" the sequence bond breaking, network relaxation, and bond formation. Note that bonds will generally be reformed in a different microscopic configuration, as indicated by the decay of both the intensity correlation function and the macroscopic stress. Under an applied strain, after n events, the macroscopic stress measured by the rheometer drops by an amount $\Delta\sigma = n\delta\bar{\sigma}$, with $\delta\bar{\sigma}$ the average drop per event of the macroscopic stress. We further assume $\delta\bar{\sigma}$ to be proportional to the macroscopic stress acting on the gel: $\delta\bar{\sigma} = B\sigma(t)$, with $B << 1$ a numerical prefactor. B accounts for the fraction of the sample volume that no longer contributes to the elastic response of the gel after one rearrangement event. This expression may be further simplified to $\delta\bar{\sigma} = B\gamma_0 G_0$, since we focus on the accelerated regime, at small t, over which the macroscopic stress drop is small compared to the initial stress (typically, a fraction of Pa vs. several Pa; Figs. 3*A* and *D* and 4*D*), such that $\sigma(t) \approx \sigma(0) = \gamma_0 G_0$, with G_0 the gel elastic modulus.

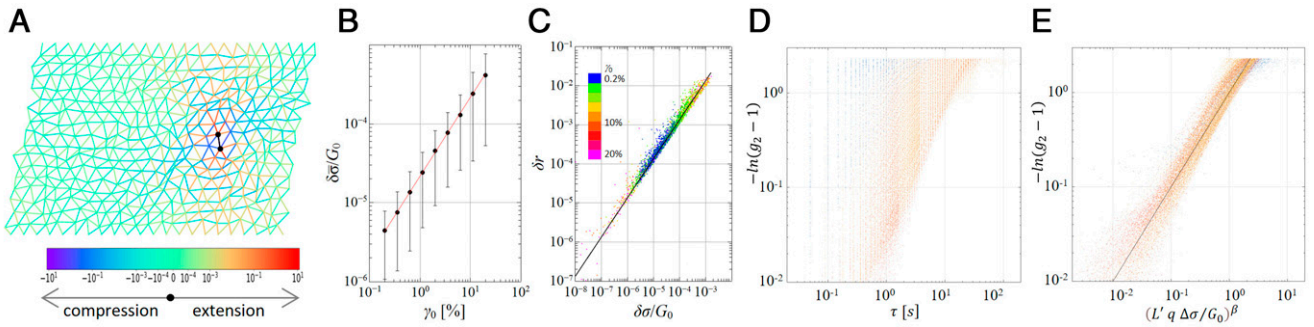

Fig. 5. Spring network simulations and comparison with the experiments validate the model. (*A*) Snapshot of a network of springs subject to a macroscopic strain $\gamma_0 = 20\%$. The springs are shown as lines whose color indicates the local strain (in percent) following the relaxation of the spring in black, to mimic a bond-breaking and bond-reforming event. (*B*) Linear dependence of the normalized stress drop per event on the applied strain. (*C*) Linear dependence of the rms displacement of network nodes vs. normalized stress drop. (*D*) Experimental intensity correlation functions vs. time delay τ during the enhanced dynamics phase in a representation convenient for the comparison with the model. Blue, red, and yellow shades are XPCS, DLS strain-ramp, and DLS step-strain data, respectively. (*E*) Same data as in *D*, plotted as a function of the normalized stress drop, using the L' and β values shown in Table 1. All data collapse on the line that shows the model prediction.

Each event entails the elastic relaxation of the network, whose components undergo a microscopic root mean square (rms) displacement $\delta\bar{r}$. After n events, the cumulated rms displacement is $\Delta r = n^p \delta\bar{r}$, where the exponent p accounts for the nature of the dynamics. Two limiting cases are diffusive dynamics, where the displacements due to successive events are totally uncorrelated ($p = 0.5$), and ballistic dynamics, where subsequent events locally displace the network along the same direction ($p = 1$). Finally, we assume that the microscopic response to a rearrangement event is ruled by linear elasticity, implying $\delta\bar{r} = \frac{L}{G_0}\delta\bar{\sigma}$, where L is a microscopic length scale.

The decay of the correlation function after n events leading to a typical displacement Δr may quite generally be written as $g_2(\Delta r) - 1 = \exp\left[-A(qn^p\delta\bar{r})^\beta\right]$, where A and β are parameters of order unity accounting for the probability distribution of the displacements (*SI Appendix*). Using the above expressions, we recast $g_2 - 1$ as a function of the macroscopic stress drop and imposed strain:

$$g_2(\Delta\sigma, \gamma_0) - 1 = \exp\left[-A(Lq)^\beta \left(\frac{\Delta\sigma}{G_0}\right)^{p\beta} (\gamma_0 B)^{\beta(1-p)}\right]. \quad [1]$$

This general result considerably simplifies for ballistic dynamics ($p = 1$), since the explicit dependence on γ_0 drops out, and Eq. **1** reduces to

$$g_2(\Delta\sigma) - 1 = \exp\left[-\left(\frac{qL'}{G_0}\right)^\beta \Delta\sigma^\beta\right], \quad [2]$$

where we have incorporated the constant A into the characteristic length $L' \equiv A^{1/\beta}L$. In our experiments, we find that $g_2 - 1$ only depends on $\Delta\sigma$, not on γ_0 (Fig. 4). Furthermore, in the XPCS experiments, we find $\Gamma \sim q$. Both results are consistent with ballistic dynamics. In the following, we shall thus take $p = 1$ and use the simpler form of the model, Eq. **2**.

Spring Network Simulations Validate the Model Assumptions. To test the key assumptions used to derive the model, $\delta\bar{r} \propto \delta\bar{\sigma}/G_0$ and $\delta\bar{\sigma} \propto \gamma_0 G_0$, we simulate the gel elastic response to a single rearrangement event using two-dimensional (2D) spring networks (Fig. 5*A*). In the simulations, an event consists of passivating a randomly chosen spring, relaxing the network, and restoring the spring in a neutral configuration (see *Materials and Methods* for details). Fig. 5*B* demonstrates that $\delta\bar{\sigma} = B\gamma_0 G_0$, as assumed in the model. Furthermore, we find $B = 2.15 \times 10^{-3}$ (expressing strain in absolute units), of the same order of magnitude as 0.91×10^{-3}, the fraction of the sample volume that is relaxed by passivating 1 out of the 1,100 simulated springs. Fig. 5*C* shows the linear relationship between the microscopic displacement upon a rearrangement event and the associated macroscopic stress drop, by displaying the individual displacements δr for 2,668 rearrangement events in networks under strains $0.2\% \leq \gamma_0 \leq 20\%$. By fitting the data to a straight line, $\delta r = L\delta\sigma/G_0$, we find $L = 13.05$, in units of the network mesh size. Finally, the simulations show that δr is isotropic and not preferentially oriented along the shear direction (*SI Appendix*).

Comparison with Experiments. We fit Eq. **2** to the data, with β and L' the fitting parameters and G_0 as directly measured by rheology. The same β and L' parameters are shared among all data collected in each of Figs. 2, 3, and 4, respectively. Fig. 5*D* shows the raw correlation functions, in a representation convenient for the comparison with the model. When plotted against the time delay τ, the correlation functions are spread over more than 2 decades in relaxation rate. Fig. 5*E* shows a remarkable collapse of the same data when plotted against $(qL'\Delta\sigma/G_0)^\beta$, as implied by Eq. **2**. Correlation functions measured over a factor of 6 in q vectors, a factor of 40 in $\dot{\gamma}$, and 2 decades in γ_0 all agree with the model, shown by the straight line in Fig. 5*E*. Table 1 shows the fitting parameters β and L': Similar values are found across all experiments, lending further support to the model.

Discussion and Conclusions

The central result of our study is the dramatic enhancement of the microscopic mucus dynamics upon applying a modest shear stress. The mucus mobility increases by up to 2 orders of magnitude and slowly relaxes to its unperturbed value over several tens of seconds. Bonds in mucus gels continuously break and reform. At first sight, the most natural explanation for the accelerated dynamics would be stress-enhanced bond dynamics, a key feature of noncovalent biomolecular interactions (52, 63). More generally, amorphous soft solids exhibit accelerated microscopic dynamics upon applying a strong mechanical drive (34–40,

Table 1. Model parameters[a] for the experiments of Figs. 2–4

Parameter[a]	XPCS, Fig. 2	DLS, Fig. 3	DLS, Fig. 4
β	1.46 ± 0.1	1.51 ± 0.1	1.33 ± 0.1
L'[μm]	12.3 ± 1	5.6 ± 0.6	4.3 ± 0.4
G_0 [Pa]	53.6	45	180

[a] β and L' are fitting parameters; G_0 is a fixed parameter obtained directly from rheology.

64, 65), a phenomenon known as "rejuvenation" and captured by models such as the soft glassy rheology (66). However, stress-induced bond dynamics and rejuvenation impact both the microscopic dynamics and the macroscopic mechanical response: As such, they are distinctive features of the nonlinear viscoelastic regime. By contrast, the enhanced dynamics reported here occur in the linear viscoelastic regime. Our model rationalizes them with no need of invoking enhanced bond dynamics, which would be incompatible with linear viscoelasticity. The key ingredients of the model are network elasticity and bond breaking: The dynamics are due to the elastic strain field generated within the network when a bond is broken. Our experiments indicate that the dynamics are ballistic. This suggests correlations between successive rearrangement events, resulting in local displacements of the gel network along the same direction over several events, in analogy to modeling and numerical results for the spontaneous dynamics of gel networks due to internal stresses (53, 67).

By fitting the model to the data, we identify a length scale L of the order of several micrometers that characterizes the elastic propagation of the microscopic strain field set by one single event. Interestingly, this length scale is close to important structural length scales highlighted in previous works. In ref. 14, pig gastric mucus was shown to exhibit fractal morphology up to ≈ 3 μm, beyond which its structure became rather uniform. The largest pores in respiratory mucus have a comparable size (68). Pig mucus covering the airways is mainly composed by gel-forming mucins MUC5B and MUC5AC, which were recently shown to be produced by goblet cells and submucosal glands in distinct morphological structures (strands, threads, and sheets), with cross-sections on the order of a few micrometers (69). Our results suggest that these structural length scales may also have a relevance for the mechanical response of mucus at the microscopic level. Note that our model invokes linear elastic response: The emerging length scale L is also consistent with ≈ 10 μm, the cross-over length scale above which microrheology experiments recover the macroscopic mechanical behavior (7, 8, 16).

Our finding that even a modest stress greatly enhances the microscopic dynamics may help in understanding why, on micrometer scales, mucus is reorganized to a greater extent compared to expectations from macroscopic rheology. Celli et al. (24) estimate the stress exerted by the mucus-penetrating bacterium *Helicobacter pylori* to be around 1 Pa, 1 decade smaller than the macroscopic yield stress of mucus. The stress-induced enhancement of the mucus dynamics reported here may be an additional factor allowing for bacterial penetration, together with the alteration of the rheological properties of mucus due to chemicals released by the bacterium (24). Other processes for which a stress-induced enhancement of the microscopic dynamics may be relevant include cilia beating and the transport through mucus of nanoparticle-based drug vectors. The mechanisms invoked to rationalize our findings rely only on the notion of nonpermanent bonds and linear elasticity: We thus expect the phenomenology reported here to be generic to out-of-equilibrium physical gels. More generally, we expect similar mechanisms to be relevant to the microscopic dynamics of mechanically driven soft solids, in both the linear and nonlinear viscoelastic regime, since any local rearrangement will entail an elastic strain field whose magnitude depends on the externally applied stress. Further experiments will be needed to test these hypotheses in mucus gels and other soft solids.

Materials and Methods

Mucus Samples. Samples were collected from the stomach of just-slaughtered pigs, extensively washed with water, and immediately frozen, with no further purification or homogenization treatments. Before testing, a fragment of the stomach was thawed and scraped to collect the sample. Sodium azide (0.02% weight concentration [wt/wt]) was added to prevent bacterial growth. The sample pH was 5.8 ± 0.5, and the dry fraction ranged from 9 to 15.5%, depending on sample.

Rheology. The measurements of Fig. 1 were performed on a Thermo Scientific Haake Mars III rheometer, equipped with a cone and plate tool (cone angle: 1°, diameter 30 mm). Stress-relaxation data simultaneous to the XPCS measurements of Fig. 2 were obtained by using a Haake RS6000 rheometer, equipped with a plate–plate tool [plate diameter: $2R = 20$ mm, gap: $e = 1$ mm (70)]. All other data were obtained on an Anton Paar MCR502 rheometer equipped with glass plate–plate tools, with $2R = 50$ mm and $e = 0.3$ mm. In all tests, mucus was loaded in the rheometer preheated at 37 °C and left at rest for at least 20 min to erase any stress induced by loading. A thin layer of silicone oil was deposited on the sample rim to prevent water evaporation. Note that in the plate–plate geometry, both the strain and the stress increase linearly with distance from the tool axis (71). In this work, γ_0 and σ refer to the strain and stress at the location where the microscopic dynamics are measured.

Rheo-XPCS and Rheo-DLS Measurements. XPCS measurements were performed at the ID02 beamline of the European Synchrotron Radiation Facility (ESRF), by using a partially coherent X-ray beam with wavelength $\lambda = 9.95 \times 10^{-2}$ nm and cross-section 20×20 μm^2 and an Eiger 500K camera at distance d from the sample as a detector. The mucus spontaneous dynamics (Fig. 2*A*) were measured at $d = 20$ m, by loading the sample in a glass capillary. Coupled rheo-XPCS measurements were performed in the tangential geometry, where the X-ray beam passes through the sample near the edge of the plate–plate tool (*SI Appendix*). For the rheo-XPCS measurements, d was set to 30.7 m, and a small amount of silica particles was added to the sample to enhance the scattering contrast [Ludox TM50 by Aldrich, radius ~ 18 nm (72), 1.25% wt/wt], with no change of the rheological properties (*SI Appendix*). Images of the scattered light were processed according to standard methods (ref. 73 and *SI Appendix*) to calculate the two-time intensity correlation $g_2(t, \tau, q) - 1$, averaged over a set of scattering vectors $\mathbf{q}$ with nearly the same magnitude $4\pi\lambda^{-1}\sin(\theta/2)$ but different azimuthal orientation, with θ as the scattering angle.

Rheo-DLS measurements were performed on bare mucus (no added particles) by using a custom setup (61), as detailed in *SI Appendix*. In brief, the sample was illuminated through the transparent bottom plate of the rheometer by a laser beam with $\lambda = 532.5$ nm. Images of the backscattered light were collected by a complementary metal-oxide-semiconductor (CMOS) camera, corresponding to a scattering vector $\mathbf{q}$, whose vertical component, parallel to the rheometer axis, accounts for 90% of the overall magnitude of $\mathbf{q}$, $q = 33$ μm^{-1}. For the data of Fig. 3, two-time intensity correlation functions $g_2(t, \tau, q = 33\ \mu\text{m}^{-1})$ were averaged over the full field of view, corresponding to a cylindrical sample volume of radius 5 mm and thickness $e = 0.3$ mm, located at $\simeq 17$ mm from the tool axis. The data of Fig. 4 were collected by imaging the whole rheometer plate. The correlation functions were averaged over nine rings of pixel, corresponding to growing values of the radial distance from the rheometer axis and thus of σ and γ_0.

Simulations. The 2D spring networks were used to simulate the response of a sheared elastic network to a bond-breaking event. The networks comprise 1,100 springs, initially placed on a triangular lattice with lattice parameter a. Periodic boundary conditions were implemented in the x direction. The nodes of the first and last row had fixed y coordinates, $y = 0$ and $y = y_{max}$, respectively, and were connected only to nodes in the bulk. Initial configurations were obtained by displacing in the x direction the upper row of nodes by an amount $\gamma_0 y_{max}$, thereby applying a constant shear γ_0. The network was then relaxed by minimizing the total elastic energy with respect to the position of the nodes in the bulk. The energy minimization was implemented in a custom Python code by using the SciPy *minimize* function (38). Disorder was introduced by randomly drawing the spring-rest lengths l_0 and spring constants k from Gaussian distributions, with $< l_0 >= a$ and typical relative SD $\sigma_{l_0}/a = \sigma_k/ < k >= 0.25$. We checked that the results did not depend on the details of the probability density function, in the limit of moderate disorder (relative SD < 0.5).

Rearrangement events were simulated as pairs of bond-breaking and bond-forming events. Bond breaking was mimicked by randomly choosing a spring i of the sheared system, setting $k_i = 0$, and relaxing the network configuration. The same bond was then reformed in an unstrained state, by setting the spring-rest length to the bond length in the new configuration. Finally, the spring constant k_i was set back to its value prior to the rearrangement event. This procedure mimics new bonds that, following a bond-breaking event, form in a relaxed state and thus do not require elastic energy to be input to the system. These new bonds, however, will contribute to the network elasticity in response to further bond-breaking events.

We measured the change of the shear stress, $\delta\sigma_{xy}$, and the rms displacement of the bulk nodes, δr, following one event. Here, $\delta r = \sqrt{\delta x^2 + \delta y^2}$, with δx and δy the rms displacements of the bulk nodes along the x and y direction, respectively. The shear stress is defined as the x component of the force per node acting on the upper and lower lattice rows, measured in units of $< k >$. We found that relaxing a spring oriented nearly parallel to the plates entailed a negligible stress drop $\delta\sigma_{xy}$. We thus restricted our analysis to rearrangement events involving springs that form an angle larger than 20° with the plates. We found isotropic response, $\delta x^2 \approx \delta y^2 \approx 0.5\delta r^2$. All displacements are expressed in units of a. The results shown in Fig. 5 have been obtained for both pristine networks and networks that previously underwent up to 500 rearrangement events.

Data Availability. ASCII and Excel files for all the datasets shown in the figures of the main text and *SI Appendix* have been deposited in Zenodo (DOI: 10.5281/zenodo.5533877) (74).

ACKNOWLEDGMENTS. We thank J.-L. Barrat for insightful discussions. We acknowledge the ESRF for provision of synchrotron radiation facilities and thank T. Narayan and L. Sharpnack for assistance in using Beamline ID02. This work was supported by French Centre National D'Etudes Spatiales, CNRS, Agence Nationale de la Recherche Grants ANR-14-CE32-0005, Failure Precursors in Soft Matter, and ANR-20-CE06-0028, MultiNet; and Association Nationale de la Recherche et de la Technologie Grant 2014/0109. L.C. was supported by the Institut Universitaire de France.

1. M. W. Denny, Invertebrate mucous secretions: Functional alternatives to vertebrate paradigms. *Symp. Soc. Exp. Biol.* **43**, 337–366 (1989).
2. P. A. Vasquez, M. G. Forest, "Complex fluids and soft structures in the human body" in *Complex Fluids in Biological Systems*, S. E. Spagnolie, Ed. (Biological and Medical Physics, Biomedical Engineering, Springer Science + Business Media, New York, 2015), pp. 53–110.
3. R. A. Cone, Barrier properties of mucus. *Adv. Drug Deliv. Rev.* **61**, 75–85 (2009).
4. R. Bansil, B. S. Turner, Mucin structure, aggregation, physiological functions and biomedical applications. *Curr. Opin. Colloid Interface Sci.* **11**, 164–170 (2006).
5. C. E. Wagner, K. M. Wheeler, K. Ribbeck, Mucins and their role in shaping the functions of mucus barriers. *Annu. Rev. Cell Dev. Biol.* **34**, 189–215 (2018).
6. C. Ridley, D. J. Thornton, Mucins: The frontline defence of the lung. *Biochem. Soc. Trans.* **46**, 1099–1106 (2018).
7. O. W. Meldrum *et al.*, Mucin gel assembly is controlled by a collective action of non-mucin proteins, disulfide bridges, Ca^{2+}-mediated links, and hydrogen bonding. *Sci. Rep.* **8**, 1–16 (2018).
8. S. K. Lai, Y. Y. Wang, D. Wirtz, J. Hanes, Micro- and macrorheology of mucus. *Adv. Drug Deliv. Rev.* **61**, 86–100 (2009).
9. L. Cohn, Mucus in chronic airway diseases: Sorting out the sticky details. *J. Clin. Invest.* **116**, 306–308 (2006).
10. P. Georgiades, P. D. A. Pudney, D. J. Thornton, T. A. Waigh, Particle tracking microrheology of purified gastrointestinal mucins. *Biopolymers* **101**, 366–377 (2014).
11. J. R. Stokes, W. J. Frith, Rheology of gelling and yielding soft matter systems. *Soft Matter* **4**, 1133–1140 (2008).
12. M. W. Denny, J. M. Gosline, The physical properties of the pedal mucus of the terrestrial slug, *Ariolimax columbianus*. *J. Exp. Biol.* **88**, 375–394 (1980).
13. M. W. Denny, "Molecular biomechanics of molluscan mucous secretions" in *The Mollusca, Vol. I: Metabolic Biochemistry and Molecular Biomechanics*, P. W. Hochachka, Ed. (Elsevier, Amsterdam, 1983), vol. **1**, pp. 431–465.
14. A. M. Philippe, L. Cipelletti, D. Larobina, Mucus as an arrested phase separation gel. *Macromolecules* **50**, 8221–8230 (2017).
15. A. Macierzanka *et al.*, Transport of particles in intestinal mucus under simulated infant and adult physiological conditions: Impact of mucus structure and extracellular DNA. *PLoS One* **9**, e95274 (2014).
16. W. J. Weigand *et al.*, Active microrheology determines scale-dependent material properties of *Chaetopterus mucus*. *PLoS One* **12**, e0176732 (2017).
17. C. E. Wagner, B. S. Turner, M. Rubinstein, G. H. McKinley, K. Ribbeck, A rheological study of the association and dynamics of MUC5AC gels. *Biomacromolecules* **18**, 3654–3664 (2017).
18. B. Demouveaux, V. Gouyer, F. Gottrand, T. Narita, J. L. Desseyn, Gel-forming mucin interactome drives mucus viscoelasticity. *Adv. Colloid Interface Sci.* **252**, 69–82 (2018).
19. M. Jory *et al.*, Mucus microrheology measured on human bronchial epithelium culture. *Front. Phys.* **7**, 19 (2019).
20. T. G. Mason, D. A. Weitz, Optical measurements of frequency-dependent linear viscoelastic moduli of complex fluids. *Phys. Rev. Lett.* **74**, 1250–1253 (1995).
21. B. H. Bajka, N. M. Rigby, K. L. Cross, A. Macierzanka, A. R. Mackie, The influence of small intestinal mucus structure on particle transport ex vivo. *Colloids Surf. B Biointerfaces* **135**, 73–80 (2015).
22. M. M. Norton, R. J. Robinson, S. J. Weinstein, Model of ciliary clearance and the role of mucus rheology. *Phys. Rev. E Stat. Nonlin. Soft Matter Phys.* **83**, 011921 (2011).
23. N. Figueroa-Morales, L. Dominguez-Rubio, T. L. Ott, I. S. Aranson, Mechanical shear controls bacterial penetration in mucus. *Sci. Rep.* **9**, 9713 (2019).
24. J. P. Celli *et al.*, *Helicobacter pylori* moves through mucus by reducing mucin viscoelasticity. *Proc. Natl. Acad. Sci. U.S.A.* **106**, 14321–14326 (2009).
25. M. King, The role of mucus viscoelasticity in cough clearance. *Biorheology* **24**, 589–597 (1987).
26. S. S. Datta, A. Preska Steinberg, R. F. Ismagilov, Polymers in the gut compress the colonic mucus hydrogel. *Proc. Natl. Acad. Sci. U.S.A.* **113**, 7041–7046 (2016).
27. B. Button *et al.*, A periciliary brush promotes the lung health by separating the mucus layer from airway epithelia. *Science* **337**, 937–941 (2012).
28. W. H. Anderson *et al.* The relationship of mucus concentration (hydration) to mucus osmotic pressure and transport in chronic bronchitis. *Am. J. Respir. Crit. Care Med.* **192**, 182–190 (2015).
29. R. H. Ewoldt, C. Clasen, A. E. Hosoi, G. H. McKinley, Rheological fingerprinting of gastropod pedal mucus and synthetic complex fluids for biomimicking adhesive locomotion. *Soft Matter* **3**, 634–643 (2007).
30. K. Hyun *et al.*, A review of nonlinear oscillatory shear tests: Analysis and application of large amplitude oscillatory shear (LAOS). *Prog. Polym. Sci.* **36**, 1697–1753 (2011).
31. D. Coblas, D. Broboana, C. Balan, Correlation between large amplitude oscillatory shear (LAOS) and steady shear of soft solids at the onset of the fluid rheological behavior. *Polymer (Guildf.)* **104**, 215–226 (2016).
32. D. Bonn, M. M. Denn, L. Berthier, T. Divoux, S. Manneville, Yield stress materials in soft condensed matter. *Rev. Mod. Phys.* **89**, 035005 (2017).
33. G. J. Donley, P. K. Singh, A. Shetty, S. A. Rogers, Elucidating the G'' overshoot in soft materials with a yield transition via a time-resolved experimental strain decomposition. *Proc. Natl. Acad. Sci. U.S.A.* **117**, 21945–21952 (2020).
34. V. Viasnoff, F. Lequeux, Rejuvenation and overaging in a colloidal glass under shear. *Phys. Rev. Lett.* **89**, 065701 (2002).
35. P. Schall, D. A. Weitz, F. Spaepen, Structural rearrangements that govern flow in colloidal glasses. *Science* **318**, 1895–1899 (2007).
36. M. C. Rogers *et al.*, Echoes in x-ray speckles track nanometer-scale plastic events in colloidal gels under shear. *Phys. Rev. E Stat. Nonlin. Soft Matter Phys.* **90**, 062310 (2014).
37. T. Sentjabrskaja *et al.*, Creep and flow of glasses: Strain response linked to the spatial distribution of dynamical heterogeneities. *Sci. Rep.* **5**, 1–11 (2015).
38. P. Virtanen *et al.*; SciPy 1.0 Contributors, SciPy 1.0: Fundamental algorithms for scientific computing in Python. *Nat. Methods* **17**, 261–272 (2020).
39. S. Aime, L. Ramos, L. Cipelletti, Microscopic dynamics and failure precursors of a gel under mechanical load. *Proc. Natl. Acad. Sci. U.S.A.* **115**, 3587–3592 (2018).
40. M. C. Rogers *et al.*, Microscopic signatures of yielding in concentrated nanoemulsions under large-amplitude oscillatory shear. *Phys. Rev. Mater.* **2**, 095601 (2018).
41. R. Pastore, C. Siviello, F. Greco, D. Larobina, Anomalous aging and stress relaxation in macromolecular physical gels: The case of strontium alginate. *Macromolecules* **53**, 649–657 (2020).
42. C. Siviello, F. Greco, D. Larobina, Analysis of linear viscoelastic behaviour of alginate gels: Effects of inner relaxation, water diffusion, and syneresis. *Soft Matter* **11**, 6045–6054 (2015).
43. C. Siviello, F. Greco, D. Larobina, Analysis of the aging effects on the viscoelasticity of alginate gels. *Soft Matter* **12**, 8726–8735 (2016).
44. R. R. Hartley, R. P. Behringer, Logarithmic rate dependence of force networks in sheared granular materials. *Nature* **421**, 928–931 (2003).
45. J. Brujić *et al.*, Granular dynamics in compaction and stress relaxation. *Phys. Rev. Lett.* **95**, 128001 (2005).
46. M. Siebenbürger, M. Ballauff, T. Voigtmann, Creep in colloidal glasses. *Phys. Rev. Lett.* **108**, 255701 (2012).
47. K. Suman, Y. M. Joshi, Analyzing onset of nonlinearity of a colloidal gel at the critical point. *J. Rheol. (N.Y.N.Y.)* **63**, 991–1001 (2019).
48. K. Hyun *et al.*, Fourier-transform rheology under medium amplitude oscillatory shear for linear and branched polymer melts. *J. Rheol. (N.Y.N.Y.)* **51**, 1319–1342 (2007).
49. B. Berne, R. Pecora, *Dynamic Light Scattering: With Applications to Chemistry, Biology, and Physics* (Wiley, Hoboken, NJ, 1976).
50. L. Cipelletti, S. Manley, R. C. Ball, D. A. Weitz, Universal aging features in the restructuring of fractal colloidal gels. *Phys. Rev. Lett.* **84**, 2275–2278 (2000).
51. A. Madsen, R. L. Leheny, H. Guo, M. Sprung, O. Czakkel, Beyond simple exponential correlation functions and equilibrium dynamics in x-ray photon correlation spectroscopy. *New J. Phys.* **12**, 055001 (2010).
52. O. Lieleg, J. Kayser, G. Brambilla, L. Cipelletti, A. R. Bausch, Slow dynamics and internal stress relaxation in bundled cytoskeletal networks. *Nat. Mater.* **10**, 236–242 (2011).
53. M. Bouzid, J. Colombo, L. V. Barbosa, E. Del Gado, Elastically driven intermittent microscopic dynamics in soft solids. *Nat. Commun.* **8**, 1–8 (2017).
54. S. Tang, M. Wang, B. D. Olsen, Anomalous self-diffusion and sticky Rouse dynamics in associative protein hydrogels. *J. Am. Chem. Soc.* **137**, 3946–3957 (2015).
55. I. Mahmad Rasid, N. Holten-Andersen, B. D. Olsen, Anomalous diffusion in associative networks of high-sticker-density polymers. *Macromolecules* **54**, 1354–1365 (2021).
56. J. P. Bouchaud, E. Pitard, Anomalous dynamical light scattering in soft glassy gels. *Eur. Phys. J. E* **6**, 231–236 (2001).
57. J. P. Bouchaud, *Anomalous Relaxation in Complex Systems: From Stretched to Compressed Exponentials in Anomalous Transport* (John Wiley & Sons, Ltd., Hoboken, NJ, 2008), pp. 327–345.

58. A. H. Krall, D. A. Weitz, Internal dynamics and elasticity of fractal colloidal gels. *Phys. Rev. Lett.* **80**, 778 (1998).
59. P. Barretta, F. Bordi, C. Rinaldi, G. Paradossi, A dynamic light scattering study of hydrogels based on telechelic poly(vinyl alcohol). *J. Phys. Chem. B* **104**, 11019–11026 (2000).
60. M. Usuelli *et al.*, Probing the structure of filamentous nonergodic gels by dynamic light scattering. *Macromolecules* **53**, 5950–5956 (2020).
61. A. Pommella, A. M. Philippe, T. Phou, L. Ramos, L. Cipelletti, Coupling space-resolved dynamic light scattering and rheometry to investigate heterogeneous flow and nonaffine dynamics in glassy and jammed soft matter. *Phys. Rev. Appl.* **11**, 034073 (2019).
62. A. Duri, D. A. Sessoms, V. Trappe, L. Cipelletti, Resolving long-range spatial correlations in jammed colloidal systems using photon correlation imaging. *Phys. Rev. Lett.* **102**, 085702–085704 (2009).
63. E. Evans, Introductory Lecture: Energy landscapes of biomolecular adhesion and receptor anchoring at interfaces explored with dynamic force spectroscopy. *Faraday Discuss.* **111**, 1–16 (1999).
64. H. N. Lee, K. Paeng, S. F. Swallen, M. D. Ediger, Direct measurement of molecular mobility in actively deformed polymer glasses. *Science* **323**, 231–234 (2009).
65. M. Warren, J. Rottler, Deformation-induced accelerated dynamics in polymer glasses. *J. Chem. Phys.* **133**, 164513 (2010).
66. P. Sollich, F. Lequeux, P. Hébraud, M. E. Cates, Rheology of soft glassy materials. *Phys. Rev. Lett.* **78**, 2020 (1997).
67. A. Duri, L. Cipelletti, Length scale dependence of dynamical heterogeneity in a colloidal fractal gel. *Europhys. Lett.* **76**, 972–978 (2006).
68. J. Kirch *et al.*, Optical tweezers reveal relationship between microstructure and nanoparticle penetration of pulmonary mucus. *Proc. Natl. Acad. Sci. U.S.A.* **109**, 18355–18360 (2012).
69. L. S. Ostedgaard *et al.*, Gel-forming mucins form distinct morphologic structures in airways. *Proc. Natl. Acad. Sci. U.S.A.* **114**, 6842–6847 (2017).
70. T. Zinn *et al.*, Ultra-small-angle X-ray photon correlation spectroscopy using the Eiger detector. *J. Synchrotron Radiat.* **25**, 1753–1759 (2018).
71. C. W. Macosko, *Rheology: Principles, Measurements, and Applications* (Advances in Interfacial Engineering Series, Wiley-VCH, New York, 1996).
72. D. Truzzolillo, V. Roger, C. Dupas, S. Mora, L. Cipelletti, Bulk and interfacial stresses in suspensions of soft and hard colloids. *J. Phys. Condens. Matter* **27**, 194103 (2015).
73. A. Duri, H. Bissig, V. Trappe, L. Cipelletti, Time-resolved-correlation measurements of temporally heterogeneous dynamics. *Phys. Rev. E Stat. Nonlin. Soft Matter Phys.* **72**, 051401 (2005).
74. D. Larobina, A. Pommella, A.-M. Philippe, M.-Y. Nagazi, L. Cipelletti, Data for the manuscript "Enhanced microscopic dynamics in mucus gels under a mechanical load in the linear viscoelastic regime" (PNAS). Zenodo. https://zenodo.org/search?page=1&size=20&q=cipelletti. Deposited 28 September 2021.